# Spinel materials for Li-ion batteries: new insights obtained by operando neutron and synchrotron X-ray diffraction

Matteo Bianchini, François Fauth, Emmanuelle Suard, Jean-Bernard Leriche, Christian Masquelier, Laurence Croguennec

STRUCTURAL SCIENCE CRYSTAL ENGINEERING MATERIALS

ISSN 2052-5206

# Spinel materials for Li-ion batteries: new insights obtained by *operando* neutron and synchrotron X-ray diffraction

Matteo Bianchini,[a,b,c,d] François Fauth,[e] Emmanuelle Suard,[c] Jean-Bernard Leriche,[a] Christian Masquelier[a,d,f] and Laurence Croguennec[b,d,f]*

[a]Laboratoire de Réactivité et de Chimie des Solides, CNRS-UMR#7314, Université de Picardie Jules Verne, F-80039 Amiens CEDEX 1, France, [b]CNRS, Université de Bordeaux, Bordeaux INP, ICMCB UPR 9048, F-33600 Pessac, France, [c]Institut Laue–Langevin, 71 Avenue des Martyrs, F-38000 Grenoble, France, [d]RS2E, Réseau Français sur le Stockage Electrochimique de l'Energie, FR CNRS 3459, France, [e]CELLS – ALBA synchrotron, Cerdanyola del Vallès, E-08290 Barcelona, Spain, and [f]ALISTORE-ERI European Research Institute, FR CNRS 3104, France. *Correspondence e-mail: laurence.croguennec@icmcb.cnrs.fr

Received 2 July 2015
Accepted 14 September 2015

Edited by K. Chapman, Argonne National Laboratory, USA

**Keywords:** batteries; spinel; synchrotron X-ray diffraction; neutron diffraction; *operando*.

**Supporting information**: this article has supporting information at journals.iucr.org/b

In the last few decades Li-ion batteries changed the way we store energy, becoming a key element of our everyday life. Their continuous improvement is tightly bound to the understanding of lithium (de)intercalation phenomena in electrode materials. Here we address the use of *operando* diffraction techniques to understand these mechanisms. We focus on powerful probes such as neutrons and synchrotron X-ray radiation, which have become increasingly familiar to the electrochemical community. After discussing the general benefits (and drawbacks) of these characterization techniques and the work of customization required to adapt standard electrochemical cells to an *operando* diffraction experiment, we highlight several very recent results. We concentrate on important electrode materials such as the spinels $Li_{1+x}Mn_{2-x}O_4$ ($0 \leq x \leq 0.10$) and $LiNi_{0.4}Mn_{1.6}O_4$. Thorough investigations led by *operando* neutron powder diffraction demonstrated that neutrons are highly sensitive to structural parameters that cannot be captured by other means (for example, atomic Debye–Waller factors and lithium site occupancy). Synchrotron radiation X-ray powder diffraction reveals how $LiMn_2O_4$ is subject to irreversibility upon the first electrochemical cycle, resulting in severe Bragg peak broadening. Even more interestingly, we show for the first time an ordering scheme of the elusive composition $Li_{0.5}Mn_2O_4$, through the coexistence of $Mn^{3+}$:$Mn^{4+}$ 1:3 cation ordering and lithium/vacancy ordering. More accurately written as $Li_{0.5}Mn^{3+}_{0.5}Mn^{4+}_{1.5}O_4$, this intermediate phase loses the $Fd\bar{3}m$ symmetry, to be correctly described in the $P2_13$ space group.

## 1. Introduction

Due to their industrial application as leading power sources for portable devices, Li-ion batteries (LIBs) have stimulated a huge amount of work in the last 35 years (Armand & Tarascon, 2008; Goodenough & Kim, 2010), recently boosted by the quest for high-range electric vehicles (EVs) and storage-grid applications (Yang *et al.*, 2011; Erickson *et al.*, 2014; Van Noorden, 2014; Andre *et al.*, 2015). A thorough comprehension of how a given electrode material for Li-ion batteries functions is a mandatory requirement to exploit its maximum potentialities and any attempt at improving its performances. This asks for a detailed understanding of how the crystal structure and the physical properties are modified when the material in question (an intercalation compound) is effectively used in a battery, more specifically, when lithium is inserted and/or extracted from its framework (Masquelier & Croguennec, 2013; Croguennec & Palacin, 2015). One of the

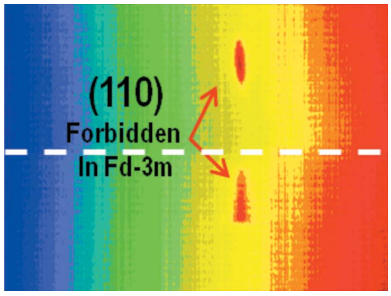

most efficient ways of achieving this is by studying the process in real time (Dahn *et al.*, 1982; Dahn, 1991; Chabre, 1993; Morcrette *et al.*, 2002). The charge–discharge of a battery is in fact a dynamical non-equilibrium process where lithium (de)intercalation, concurrently with transition metal (TM) oxidation/reduction at the positive electrode, can cause strong modifications in the crystallographic structure of the materials, which in turn can reflect on many of their physical properties. For this reason, *in situ* and *operando* studies developed quickly as soon as experimental facilities allowed them to (Harks *et al.*, 2015). Several techniques are available nowadays for such studies, often even combined to extract the maximum of the complementary information (Leriche *et al.*, 2010; Jumas *et al.*, 2013). X-ray powder diffraction (XRPD) at the laboratory scale was naturally the first technique developed and the best suited to study crystallographic changes in electrode materials, which are usually synthesized as crystalline powders (Dahn & Haering, 1981; Andersson *et al.*, 2000; Rossi Albertini *et al.*, 2001; Morcrette *et al.*, 2002; Chen *et al.*, 2002). Promising results quickly led to move towards synchrotron XRPD studies (Thurston *et al.*, 1996; Balasubramanian *et al.*, 2001; Ravnsbaek *et al.*, 2014) and, more recently, to neutron powder diffraction (NPD) ones (Bergstöm *et al.*, 1998; Colin *et al.*, 2010; Sharma & Peterson, 2012).

In this paper we give an introductory review on the state-of-the-art of *operando* neutron powder diffraction on LIBs (§2) and briefly describe our recent design of a new neutron-transparent electrochemical cell. This technique was found to be highly suitable for the precise study of the structural evolution, upon $Li^+$ extraction, from manganese-based spinel materials $Li_{1+x}Mn_{2-x}O_4$ (§3) and $LiNi_{0.4}Mn_{1.6}O_4$ (§4). These studies have been complemented by high-resolution *operando* synchrotron XRPD which gave unexpected insights on the first cycle irreversibility upon $Li^+$ extraction from $LiMn_2O_4$ and on the structure of the intermediate phase $Li_{0.5}Mn^{3+}_{0.5}Mn^{4+}_{1.5}O_4$, obtained reversibly upon charge and discharge (§5).

## 2. *Operando* neutron diffraction techniques for Li-ion batteries

The common requirement of all these characterization techniques, when carried out in real time on batteries, is the development of suitable sample environments. One hence needs an electrochemical cell able to properly function as an effective Li-ion battery and, concurrently, be able to meet the specific needs of the probing technique of choice. For X-rays and synchrotron radiation the geometry of the electrochemical cell has to accurately fit in a clearance-limited diffractometer and to be conceived with suitable windows, made of light elements, allowing X-rays to pass with low absorption and to probe the electrode material inside the cell. Advanced laboratory X-ray diffractometers sparked the development of versions of these custom-made cells and made *operando* XRPD studies rather common within the community (Morcrette *et al.*, 2002). Synchrotron XRPD (Balasubramanian *et al.*, 2001) and XAS (Cuisinier *et al.*, 2013; Koga *et al.*, 2014) techniques then became commonly exploited as well, leading to the development of various types of electrochemical cells (Baehtz *et al.*, 2005; Leriche *et al.*, 2010; Borkiewicz *et al.*, 2012; Villevieille *et al.*, 2014) suited for *operando* studies in transmission geometry. These cells exploit all the advantages of the synchrotron radiation: extremely good angular resolution, high intensity, time resolution and energy tunability.

Due to the lower availability of neutron sources and to intrinsic experimental bottlenecks related to the fundamental scattering properties of neutrons, described in the following, *operando* NPD on LIBs required more time to develop. The technique has only been seriously considered in the last 15 years, and only very recently came to a sufficient maturity (Bergstöm *et al.*, 1998; Berg *et al.*, 2001; Rosciano *et al.*, 2008; Sharma *et al.*, 2011; Sharma & Peterson, 2012; Bianchini *et al.*, 2013; Godbole *et al.*, 2013; Roberts *et al.*, 2013; Bianchini *et al.*, 2014; Vadlamani *et al.*, 2014; Pang & Peterson, 2015). The design of a cell for *operando* neutron powder diffraction indeed generates several additional difficulties with respect to X-rays. Neutron scattering is a nuclear process which is not directly related to the atomic weight of the scattering element but depends on the nuclear structure of the isotope: it is often considered to be 'randomly varying' throughout the periodic table. In this work, we do not wish to be exhaustive on the specific features of neutron scattering, for which several sources are available (Schober, 2014; Bacon, 1975). However, related to *in situ* studies on batteries, three main isotope-dependent processes are relevant and should be noted here: elastic coherent scattering, elastic incoherent scattering and neutron absorption. In the first case, neutrons are scattered coherently between different atoms, meaning that one can probe correlations among them (such a mechanism for example is at the origin of Bragg peaks in diffraction). In the second case, elastic incoherent scattering causes neutrons to be randomly scattered, originating from a strong featureless background; this is due to the isotopic distribution of a given element (namely in most cases there is no control on the actual isotope present in the sample, but elements with 'natural abundance' are used). Finally, a few elements are also strong neutron absorbers, for example lithium, boron or cadmium (*i.e.* they have at least one isotope which is a strong neutron absorber).

As a rule of thumb, to carry out a successful *operando* NPD experiment one would like to have a strong coherent signal coming from the electrode(s) under study, while minimizing the amount of incoherent scattering and neutron absorption. Unfortunately, many necessary components of LIBs such as carbon, binder and electrolytes are rich in such elements possessing a significant incoherent scattering cross section (typically hydrogen). This results in a high background, dramatically reducing the signal-to-noise ratio of the Bragg peaks of the electrode material of interest. In addition, lithium is a rather good neutron absorber, further reducing the available signal. For this reason one has to maximize the amount of electrode material illuminated by the beam, and to have the highest available neutron flux. Massive electrodes

must be prepared (> 200 mg), which makes electrochemistry often challenging. Moreover, deuterated electrolytes are often employed, although they are costly, significantly improving the signal-to-noise ratio on Bragg peaks due to the lower incoherent scattering of deuterium with respect to hydrogen (Roberts *et al.*, 2013). Despite all these difficulties, *operando* NPD is still pursued because of the great advantages of neutrons (Isnard, 2007): the high sensitivity to lithium [among the few elements with a negative scattering length ($b_{\rm Mn}^{\rm coh}$Li = −1.90 fm)], the contrast between neighbouring elements in the periodic table (*e.g.* $b_{\rm Mn}^{\rm coh}$ = −3.73 fm, while $b_{\rm Fe}^{\rm coh}$ = 9.45 fm) and the high penetrating power, allowing large portions of the battery (if not the whole) to be imaged. The fact that significant intensities are preserved at high $Q$ values [the scattering vector $Q = 4\pi\sin(\theta)/\lambda$] is another advantage distinguishing neutrons from X-rays. This allows greater sensitivity to structural parameters such as Debye–Waller factors, as we will demonstrate in the following.

Different geometries for NPD *in situ* electrochemical cells have been considered. Modified versions of every existing classic cell design have been proposed, such as swagelock-type, coin, pouch and roll-over cells, prismatic ones and some more elaborated designs. Fig. 1 gathers selected examples taken from the literature with the respective references. A review can also be found in Pang & Peterson (2015). Early versions mainly suffered from poor electrochemical properties and more recent ones do not provide sufficient data quality and/or time resolution to be treated quantitatively. Still, significant improvements have been made and to date all the most significant electrode materials have been studied at least once with *operando* NPD using custom-made cells: $LiCoO_2$ (Vadlamani *et al.*, 2014), $LiFePO_4$ (Sharma *et al.*, 2012; Bianchini *et al.*, 2013; Roberts *et al.*, 2013; Godbole *et al.*, 2013), $LiMn_2O_4$ and related spinels (Bergstöm *et al.*, 1998; Berg *et al.*, 2001; Bianchini *et al.*, 2014; Sharma *et al.*, 2013), high-voltage spinels (Pang, Sharma *et al.*, 2014), mixed layered materials (NMC and related compositions; Rosciano *et al.*, 2008; Sharma & Peterson, 2012; Godbole *et al.*, 2013; Pang, Kalluri *et al.*, 2014) and negative electrode materials ($Li_4Ti_5O_{12}$ and carbon-based; Colin *et al.*, 2010; Du *et al.*, 2011; Pang, Peterson *et al.*, 2014; Godbole *et al.*, 2013), providing significant qualitative and sometimes quantitative insight into their structural-electrochemical properties. The study of commercially available Li-ion batteries using neutrons (exploiting their high penetrating power) has also been successfully carried out, mainly to understand fatigue and failure mechanisms (Rodriguez *et al.*, 2004; Sharma *et al.*, 2010; Wang *et al.*, 2012; Cai *et al.*, 2013; Sharma & Peterson, 2013; Pang, Alam *et al.*, 2014).

## 3. A (Ti,Zr) neutron-transparent electrochemical cell and its use to study $Li_{1+x}Mn_{2-x}O_4$ spinels

The cell developed in our group is a swagelok-type electrochemical cell, manufactured with a neutron-transparent (Ti,Zr) alloy (Bianchini *et al.*, 2013). It is reported in Fig. 1(*e*). Such a design is able to isolate the electrode material of interest so as to obtain the maximum signal from it, while at the same time reducing parasitic contributions from other battery components (mainly casing and current collectors). With this cell, in combination with a deuterated electrolyte and thanks to the extremely high neutron flux available on the D20 diffractometer at Institut Laue–Langevin (Grenoble, France), we were able to obtain good-quality data and to succeed in reproducible structural refinements through the

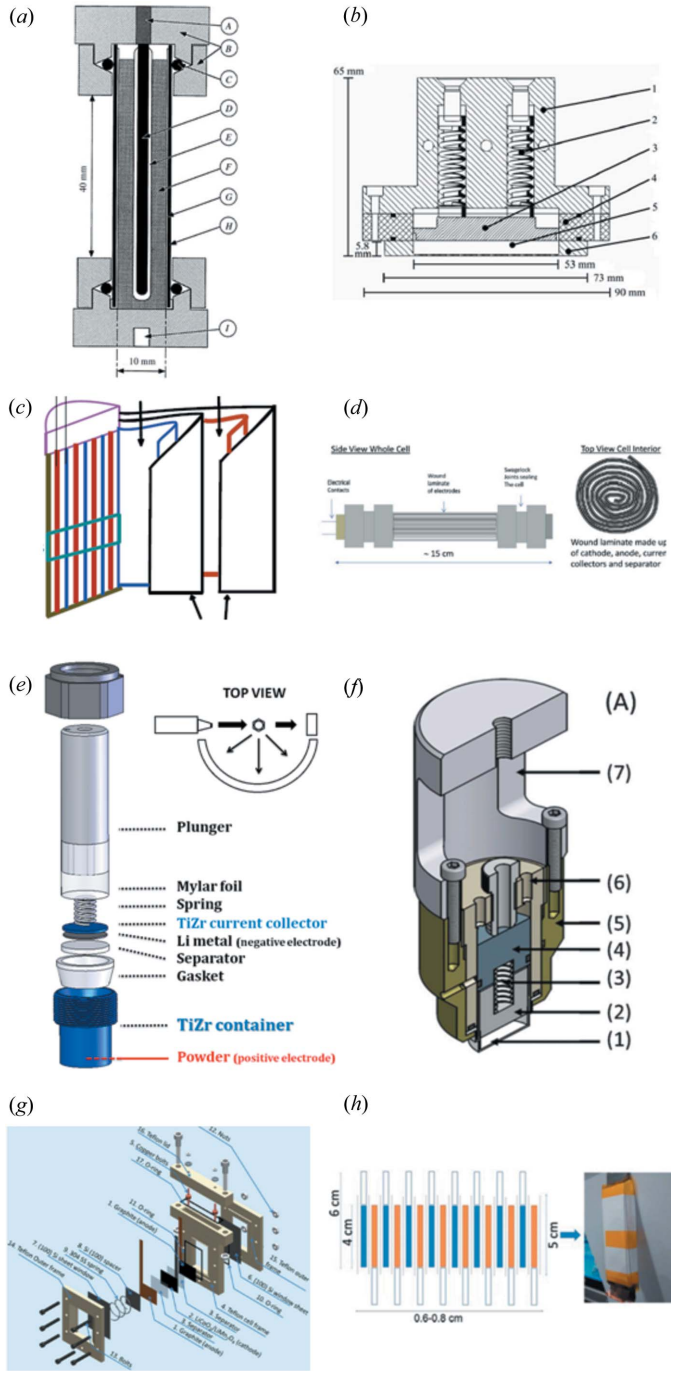


**Figure 1**
Electrochemical cells proposed for *in situ* neutron diffraction experiments. (*a*) Bergstöm *et al.* (1998), (*b*) Rosciano *et al.* (2008), (*c*) Sharma *et al.* (2011), (*d*) Roberts *et al.* (2013), (*e*) Bianchini *et al.* (2013), (*f*) Godbole *et al.* (2013), (*g*) Vadlamani *et al.* (2014), (*h*) Pang & Peterson (2015).

Rietveld method (Rietveld, 1969). We first reported on the properties of this electrochemical cell back in 2013, showing the feasibility of these analyses during a real *operando* experiment on $LiFePO_4$ as a model system (Bianchini *et al.*, 2013). Subsequently we focused on $AB_2X_4$ spinel compositions, well known in the crystallographic community since the early discovery of their crystal structure by H. W. Bragg, in parallel with S. Nishikawa, in 1915 (Bragg, 1915; Nishikawa, 1915). They are cubic, described in the space group $Fd\bar{3}m$, and interest in these materials as positive electrodes in Li-ion batteries was initially sparked by the work of M. M. Thackeray on the composition $LiMn_2O_4$ (Thackeray *et al.*, 1983, 1984; Goodenough *et al.*, 1984). Here, the *B* cation (Mn) occupies half of the octahedral sites [16*d* site in (5/8, 5/8, 5/8) with the origin at $\bar{4}3m$], and the *A* cation (Li) occupies one–eight of the tetrahedral sites, 8*a* in (0, 0, 0) (Fig. 2). Thackeray's and successive works (Tarascon *et al.*, 1991, 1995; Tarascon & Guyomard, 1993; Rousse *et al.*, 1999) clearly demonstrated the interest of this positive electrode, able to exchange one $Li^+$ ion through a sequence of two flat voltage-composition plateaus, around 4.05 and 4.15 V *versus* $Li^+/Li$ (Thackeray *et al.*, 1992; Rossouw *et al.*, 1990; Thackeray, 1997; Tarascon *et al.*, 1991). It can also intercalate a second $Li^+$ ion at $\sim 3$ V, causing a strong Jahn–Teller distortion of the lattice, deleterious to the long-term capacity retention of the battery (Cho & Thackeray, 1999; Amatucci *et al.*, 2001). Thorough control of the synthesis conditions of these apparently simple oxides was revealed to be extremely important. Typically, a slight departure from the original oxidation state of manganese (+3.5) towards the value +4 led to better capacity retention, at the expense of theoretical capacity (Gummow *et al.*, 1994; Thackeray, 1997; Tarascon & Guyomard, 1993; Tarascon *et al.*, 1994, 1995). One of the routes undertaken to achieve this result is to synthesize members of the overstoichiometric family $Li_{1+x}Mn_{2-x}O_4$ ($0 \leq x \leq 0.33$; Gummow *et al.*, 1994; Masquelier *et al.*, 1996; Kanno *et al.*, 1999), where the extra lithium ions sit in the 16*d* manganese crystallographic site.

Only a few studies have addressed the mechanism of $Li^+$ extraction from these compositions by means of *ex situ* and *in situ* X-ray diffraction (Ohzuku *et al.*, 1990; Baehtz *et al.*, 2005; Liu *et al.*, 1998; Mukerjee *et al.*, 1998). We recently performed an *operando* NPD study during the extraction of lithium from $Li_{1+x}Mn_{2-x}O_4$ spinels, with the goal of giving quantitative information about the different phases involved and with special attention being paid to lithium's site occupancy factors (SOFs). To this end, we synthesized three samples of nominal stoichiometries $LiMn_2O_4$ ($x = 0$), $Li_{1.05}Mn_{1.95}O_4$ ($x = 0.05$) and $Li_{1.10}Mn_{1.90}O_4$ ($x = 0.10$) (Bianchini *et al.*, 2014). We determined:

(i) The phase diagram of the three materials upon lithium extraction (Fig. 2), confirming that while $Li_{1.10}Mn_{1.90}O_4$ reacts through a solid solution monophasic process, $LiMn_2O_4$ undergoes two biphasic reactions upon charge with an intermediate phase close to $Li_{0.5}Mn_2O_4$.

(ii) The lithium's SOF and thus the amount of lithium present in the different phases involved. Moreover, a real-time experiment on $Li_{1.10}Mn_{1.90}O_4$ showed that the delithiation rate is not constant, but dependent on the electrode's state of charge.

(iii) The structural evolution of the materials. Thanks to the Rietveld method, we observed the expected decreasing trend of the cell parameter, caused by lithium extraction and consequent TM oxidation. In parallel with a rather constant oxygen fractional atomic coordinate, this translated into a progressive decrease of the Mn—O bond length.

This study clearly demonstrated how *operando* NPD allows capturing fine structural parameters of every atomic element in a crystalline electrode, with a special focus on lithium's behaviour.

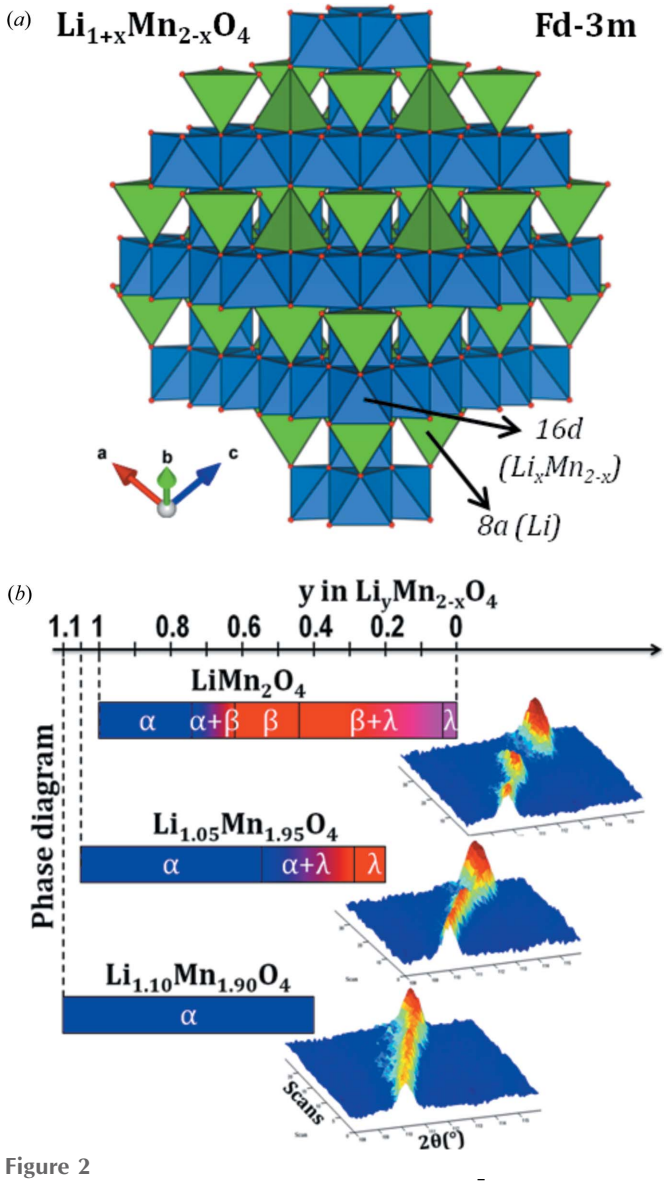


**Figure 2**
(*a*) Crystal structure of $Li_{1+x}Mn_{2-x}O_4$ in the $Fd\bar{3}m$ space group. The [111] direction is vertical, in the plane of the paper. Oxygen (red points) is in 32*e* Wyckoff positions, manganese (blue octahedra) in 16*d* ones, lithium (green tetrahedra) in 8*a* ones. The extra lithium *x* replaces Mn in 16*d* sites. Bottom: Phase diagram and Bragg peak's shift for the samples $Li_{1+x}Mn_{2-x}O_4$ ($x = 0$, 0.05, 0.10) obtained from *operando* NPD upon $Li^+$ extraction.

### 4. $Li^+$ extraction/insertion from/into high-voltage $LiNi_{0.4}Mn_{1.6}O_4$: *operando* NPD

The substitution of different TMs for Mn in $Li(TM)_xMn_{2-x}O_4$ is an interesting path to synthesize spinel materials operating as high-voltage positive electrodes (often around 5 V *versus* $Li^+/Li$). One of the most common and widely studied choices is TM = Ni, leading to a solid solution of composition $LiNi_xMn_{2-x}O_4$ in the range $0 \leq x \leq 0.5$. The end member $x$ = 0.5 ($LiNi_{0.5}Mn_{1.5}O_4$) was first synthesized and recognized for its electrochemical and crystallographic properties around 1996 (Amine *et al.*, 1996, 1997; Gao *et al.*, 1996). Manganese is found to be completely oxidized ($Mn^{4+}$) and the electrochemical activity is thus only brought by the nickel cations, exploiting oxidation states from $Ni^{2+}$ to $Ni^{4+}$. This results in a gravimetric capacity of 147 mAh $g^{-1}$ for $LiNi_{0.5}Mn_{1.5}O_4$. The material is especially interesting when lithium is deintercalated, offering a 4.7 V potential *versus* $Li^+/Li$ and a very high energy density (Amine *et al.*, 1996, 1997; Zhong *et al.*, 1997; Gao *et al.*, 1996). Several studies were published in recent years, dealing with the many aspects of the optimization and understanding of such a material (Kunduraci & Amatucci, 2006, 2008; Patoux *et al.*, 2008; Lee & Persson, 2012; Duncan *et al.*, 2014). From the crystallographic point of view $LiNi_{0.5}Mn_{1.5}O_4$ is analogous to $LiMn_2O_4$, crystallizing in the $Fd\bar{3}m$ space group and thus having Ni and Mn randomly distributed in the 16*d* crystallographic site. For certain synthesis conditions, the Ni/Mn ratio of 1:3 can lead to a reduction in symmetry to the cubic $P4_332$ space group, due to cation charge ordering (Gryffroy *et al.*, 1991). This ordered phase has, however, poorer transport properties than the cation-disordered $Fd\bar{3}m$ phase (Kim *et al.*, 2004; Gryffroy *et al.*, 1991; Amdouni *et al.*, 2006; Wang *et al.*, 2011; Duncan *et al.*, 2014) thus showing poorer electrochemical properties and being less interesting for applications. Regarding the lithium (de)intercalation reaction at 4.7 V, most studies reported on the presence of two topotactic two-phase transitions involving three cubic phases in the ordered spinels ($P4_332$). In the disordered one, the first of the two biphasic reactions is still present, but on a narrower miscibility gap (so narrow that in fact, Pang, Sharma *et al.*, 2014, described it as a solid solution region), revealing a clear influence of the cation distributions on the phase diagram and electrochemical properties of the material (Duncan *et al.*, 2014).

Compositions within the solid solution $LiNi_xMn_{2-x}O_4$ exhibit an increasing voltage upon lithium extraction when $x$ increases, while the gravimetric capacity is reduced as Ni is heavier than Mn. A good trade-off is found for $x$ = 0.4, *i.e.* for $LiNi_{0.4}Mn_{1.6}O_4$ (*i.e.* $LiNi^{2+}_{0.4}Mn^{3+}_{0.2}Mn^{4+}_{1.4}O_4$) now widely studied as a next-generation positive electrode material for Li-ion batteries (Patoux *et al.*, 2008, 2009). The capacity originates for 20% from the $Mn^{3+}/Mn^{4+}$ redox couple (around 4.2 V *versus* $Li^+/Li$), while the remaining 80% is provided by the $Ni^{2+}/Ni^{3+}$ and $Ni^{3+}/Ni^{4+}$ couples in equal amounts at 4.7 V, as shown by electrochemical and X-ray absorption measurements (Arai *et al.*, 2013; Saravanan *et al.*, 2015; Patoux *et al.*, 2008; see Fig. 3). $LiNi_{0.4}Mn_{1.6}O_4$ exhibits low capacity fading upon cycling, high energy density and good rate capabilities, making it a more interesting choice than other compositions in the $LiNi_xMn_{2-x}O_4$ solid solution (Croguennec & Palacin, 2015).

A powerful tool to isolate the contribution of different redox couples is the inverse differential curve $(dV/dx)^{-1}$ representation of the voltage–composition profile, where a peak appears for every redox process involved. It is of great importance in the study of LIBs and it is illustrated at the bottom of Fig. 3. Even for the highly polarized voltage *versus* composition data we obtain during *in situ* NPD experiments, the derivative peaks are properly separated and highlight the successive $Mn^{3+}/Mn^{4+}$, $Ni^{2+}/Ni^{3+}$ and $Ni^{3+}/Ni^{4+}$ features involved upon $Li^+$ extraction from $LiNi_{0.4}Mn_{1.6}O_4$.

The mechanism of $Li^+$ deintercalation from $LiNi_{0.4}Mn_{1.6}O_4$ is described as a solid solution, followed by a biphasic reaction

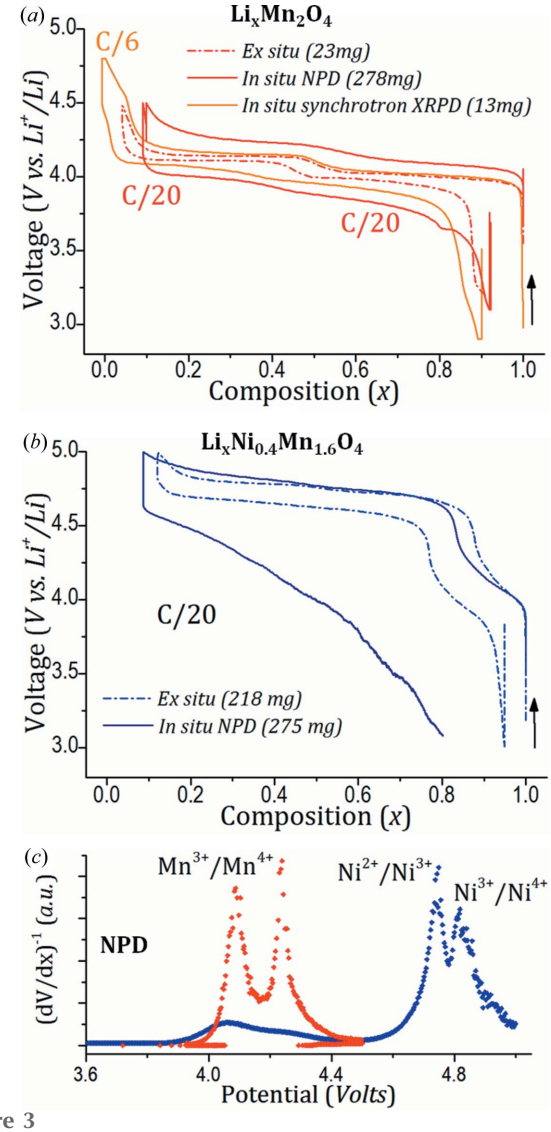


**Figure 3**
(*a*) Electrochemical voltage–composition curves obtained *ex situ* and during *in situ* NPD and *in situ* synchrotron radiation XRPD experiments for $LiMn_2O_4$. (*b*) Electrochemical voltage–composition curves obtained *ex situ* and during *in situ* NPD for $LiNi_{0.4}Mn_{1.6}O_4$. (*c*) Inverse derivative curves relative to *in situ* NPD experiments on $LiMn_2O_4$ and $LiNi_{0.4}Mn_{1.6}O_4$.

corresponding to the $Ni^{3+}/Ni^{4+}$ redox couple. Namely it behaves as a cation-disordered $LiNi_{0.5}Mn_{1.5}O_4$ spinel where the first biphasic reaction has been completely suppressed (Duncan *et al.*, 2014). To understand the mechanism behind this phase diagram and to gain insight into the deintercalation reaction, we decided to observe it in real time using *operando* NPD. A sample of $LiNi_{0.4}Mn_{1.6}O_4$ was synthesized at CEA-Liten, its composition was checked by ICP and neutron diffraction on the powder sample on the D2B diffractometer at ILL leading to $LiNi_{0.38\ (1)}Mn_{1.62\ (1)}O_4$. Our (Ti,Zr) electrochemical cell was used to cycle the material (a first charge followed by a discharge at C/20 rate, *i.e.* 1 $Li^+$ extracted or inserted in 20 h) *versus* a lithium metal negative electrode, while NPD patterns were continuously acquired for 30 min each. This means that, during both charge and discharge, a $\Delta x$ = 1/40 = 0.025 Li/scan was achieved, allowing a sufficient resolution in the electrode's composition. Charging the material up to 5 V was challenging as normal electrolytes (including our deuterated one) already tend to decompose/oxidize at such high voltage. A new deuterated electrolyte formulation has recently been proposed, which may possibly improve the high-voltage stability (Petibon *et al.*, 2015). The electrochemical data obtained during our experiment are shown in Fig. 3. Upon charge we could obtain 91% of the theoretical capacity but the electrolyte was likely significantly damaged, indeed the voltage–composition profile upon subsequent discharge was badly impacted. The abundance of electrolyte allowed the reaction to proceed nonetheless and we could recover the composition $Li_{0.8}Ni_{0.4}Mn_{1.6}O_4$ at the end of the next discharge, giving meaningful results on the overall cycle. Fig. 4 shows a complete representation of the experiment.

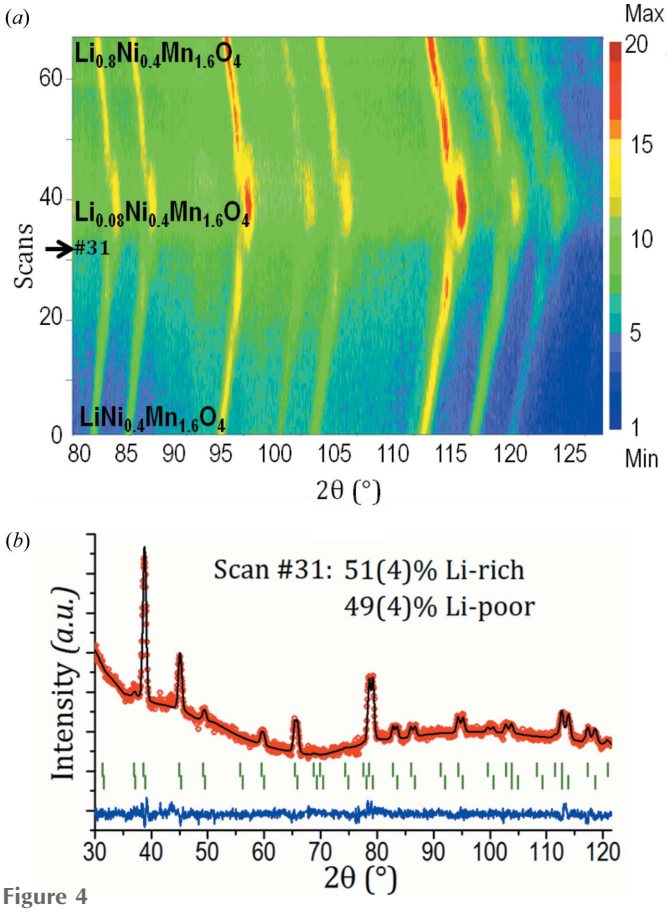


**Figure 4**
(*a*) Contour view on the first cycle of the $LiNi_{0.4}Mn_{1.6}O_4$//Li cell observed by *operando* NPD in the 80–130° angular range. The wavelength is λ = 1.54 Å. (*b*) Rietveld refinement of scan #31 during the biphasic reaction leading to Li-poor $Li_{0.08}Ni_{0.4}Mn_{1.6}O_4$.

Fig. 5 gathers the evolution of the main structural parameters and features observed through the full electrochemical cycle, summarized as follows:

(i) We confirm the existence of a solid solution region followed by a biphasic reaction upon charge. The single-phase reaction proceeds up to the composition $Li_{0.40}Ni_{0.4}Mn_{1.6}O_4$ [$Li_{0.42\ (14)}Ni_{0.4}Mn_{1.6}O_4$ from Rietveld refinement], corresponding to the full oxidation of $Mn^{3+}$ to $Mn^{4+}$ and $Ni^{2+}$ to $Ni^{3+}$. From this composition, $Li^+$ extraction occurs through a two-phase reaction involving the oxidized composition $Li_{0.08}Ni_{0.4}Mn_{1.6}O_4$ [$Li_{0.12\ (2)}Ni_{0.4}Mn_{1.6}O_4$ from Rietveld refinement]. The two processes are reversible upon discharge.

(ii) The Mn/Ni—O bond lengths significantly decrease upon charge, consistent with the TM oxidation. Similarly to the case of $Li_{1+x}Mn_{2-x}O_4$ spinels, this results mainly from the decrease of the unit-cell parameter value, while the oxygen fractional atomic coordinate inside the unit cell is poorly affected. The unit-cell parameter contracts from 8.1807 (7) to 8.057 (3) Å in the Li-rich phase ($\Delta a/a$ = 1.5%), and from 8.029 (2) to 8.0200 (3) Å in the Li-poor phase ($\Delta a/a$ = 0.1%). This induces Mn/Ni—O bonds to decrease from 1.944 (4) to 1.923 (14) Å in the Li-rich phase ($\Delta B/B$ = 1.0%), and from 1.915 (22) to 1.908 (3) Å in the Li-poor one ($\Delta B/B$ = 0.3%). Error bars fluctuate significantly, becoming large when phases are in a minority (< 20 wt%).

(iii) Lithium's SOF decreases during the Li-rich solid solution, reaching 0.42 (14) Li/f.u. The Li-poor phase instead contains 0.12 (12) Li/f.u. at the end of the charge. About 10% of lithium thus seems to remain in the structure, consistent with the fact that 91% of the theoretical capacity is measured to be obtained from the electrochemical cycling. Thanks to the use of a PTFE binder in the electrode formulation, the whole amount of spinel is electrochemically active (no residue of the pristine material is indeed observed). We thus note that the unexploited capacity is simply due to the already encountered (Baehtz *et al.*, 2005; Martinez *et al.*, 2014) difficulty in extracting the whole amount of lithium from spinels.

Interesting behaviour was observed upon close inspection of the Debye–Waller displacement parameters. In a first step, we considered $B_{iso}$ to be the same for all atoms (refining $B_{overall}$ in *FULLPROF*; Rodríguez-Carvajal, 1993) to reduce the amount of free parameters (we also refine Li SOF at this stage). We observed that $B_{overall}$ remained almost constant during the electrochemical reaction of the $Mn^{3+}/Mn^{4+}$ redox couple, while a substantial and somehow unexpected increase (more than 50%) of $B_{overall}$ was found upon oxidation of $Ni^{2+}$ into $Ni^{3+}$. During the $Ni^{3+}/Ni^{4+}$ reaction, which is biphasic, $B_{overall}$ recovers a value that is for both phases similar but slightly lower than the initial one.

Fig. 6 shows the correlation between $B_{overall}$ and electrochemistry in this experiment, *i.e.* with the inverse differential curve $(dV/dx)^{-1}$: $B_{overall}$ increases exactly as Ni cations oxidize from 2+ to 3+. To understand the reason for such an unexpected observation, we subsequently refined the Debye–Waller factors separately, while leaving other parameters fixed (including Li SOF). We could notice that the atom responsible for this increase is oxygen, and not lithium or the TMs. For example, for pattern #17 [showing the maximum value for $B_{overall}$ = 1.42 (9)] the refinement led to $B_{iso}$(O) = 1.5 (1) while $B_{iso}$(Ni/Mn) = 0.2 (2) and $B_{iso}$(Li) = 0.9 (5). $Ni^{3+}$ is a $4s^0 3d^7$ cation prone to Jahn–Teller distortion (low spin state $t_{2g}^6 e_g^1$), but too diluted by Mn in this sample to create a cooperative effect leading to a cubic-to-tetragonal transition. The distortion of the $Ni^{3+}O_6$ octahedra occurs nonetheless at the local scale, with two long and four short Ni—O bonds (typically around 2.09 and 1.91 Å as observed in $LiNiO_2$ and in $LiNi_{1/2}Mn_{1/2}O_2$, *versus* 1.90 Å for the six Mn—O bonds in $Mn^{4+}O_6$; Rougier *et al.*, 1995; Yoon *et al.*, 2003). As Ni and Mn occupy the same crystallographic site and are sitting at the centre of a regular octahedral $MO_6$ environment (as imposed by the cell description), the oxygen's $B_{iso}$ hence provides an alternative to describe how the *M*—O distances are distributed at the local scale. Upon further lithium deintercalation from $LiNi_{0.4}Mn_{1.6}O_4$ the most oxidized composition is formed with all the transition metal ions at the $Ni^{4+}$ or $Mn^{4+}$ states and, as expected, with the smaller value observed for oxygen's $B_{iso}$. Indeed, $Ni^{4+}$ and $Mn^{4+}$ are $4s^0 3d^6$ and $4s^0 3d^3$ cations stable in regular $MO_6$ octahedra with *M*—O bonds close to 1.90 Å: for that specific composition, the average *M*—O distance calculated from the Rietveld refinement is fully representative for the homogeneity of the *M*—O bonds formed at the local scale. We have thus shown that through the inspection of $B_{overall}$ (first) and oxygen's $B_{iso}$ (afterwards) in the spinel structure, *operando* NPD during electrochemical cycling can be very sensitive to subtle changes in structural parameters and enlighten local structural features.

## 5. $LiMn_2O_4$ studied by *operando* synchrotron XRPD: first cycle irreversibility, $Li^+$ and charge ordering in $Li_{0.5}Mn_2O_4$

Although the 'classical' lithium-containing spinel $LiMn_2O_4$ has been extensively investigated for approximately 30 years, certain points still remain unclear. For instance, very little is known on the nature of the elusive intermediate composition $Li_{0.5}Mn_2O_4$, found halfway through charge/discharge. This phase was first postulated as the two voltage–composition plateaus obtained upon charge are separated by only ~ 100 mV [Ohzuku *et al.*, 1990; see the two peaks in the differential curve $(dV/dx)^{-1}$ in Fig. 3]. It has been mentioned from different *in situ* studies, indexed in the same cubic space group ($Fd\bar{3}m$) as the two end members ($LiMn_2O_4$ and λ-$MnO_2$) but with different cell parameters (Thurston *et al.*, 1996; Mukerjee *et al.*, 1998; Baehtz *et al.*, 2005). Attempts to model a lithium/vacancy ordering have been made but they have never been verified experimentally (Liu *et al.*, 1998; Van der Ven *et al.*, 2000). A second yet not fully understood phenomenon concerns the capacity fading upon electrochemical cycling, commonly attributed to parasitic reactions caused by the presence of $Mn^{3+}$. A neutron diffraction experiment we undertook comparing pristine and cycled $LiMn_2O_4$ showed great difficulty in treating the Bragg peaks using the same peak shape. These data left us wondering about a possible irreversibility already present during the first cycle.

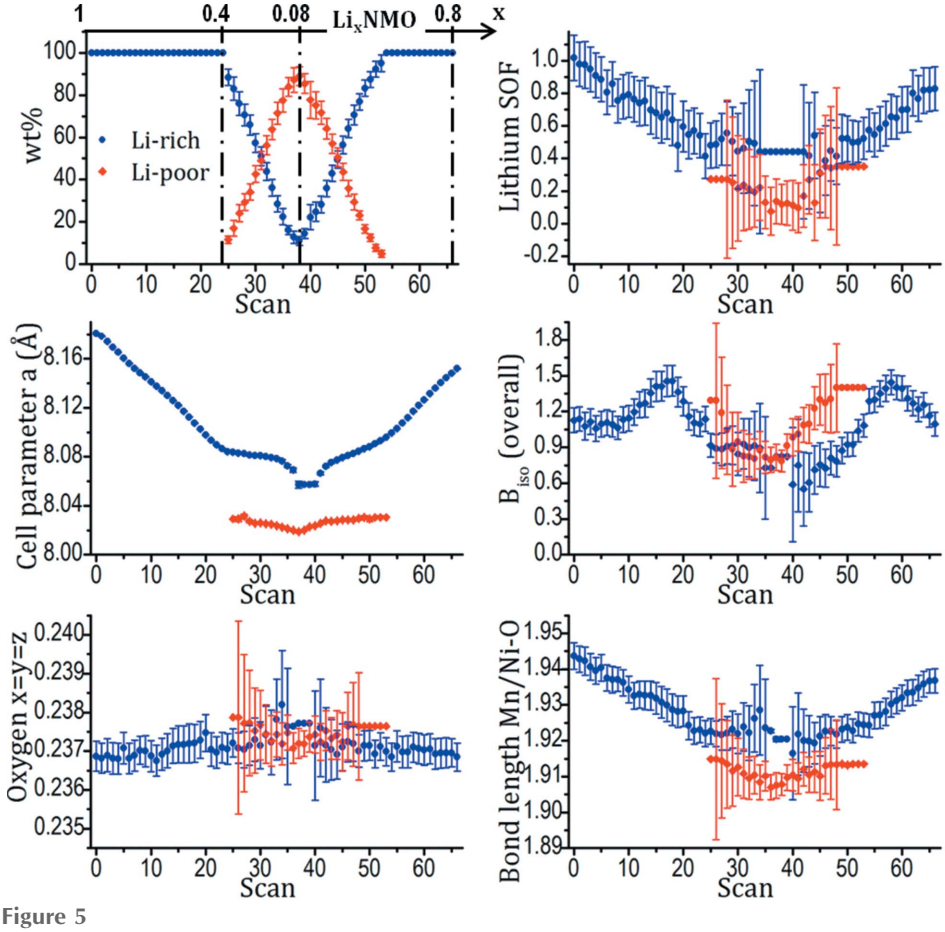


**Figure 5**
Structural parameters obtained from Rietveld refinements upon one cycle of $Li^+$ extraction/reinsertion from/into $LiNi_{0.4}Mn_{1.6}O_4$. Parameters that had been fixed do not show error bars. The *x* axis reports the scan number, which coincides with twice the time of the experiment (in hours) since every scan is recorded for 30 min.

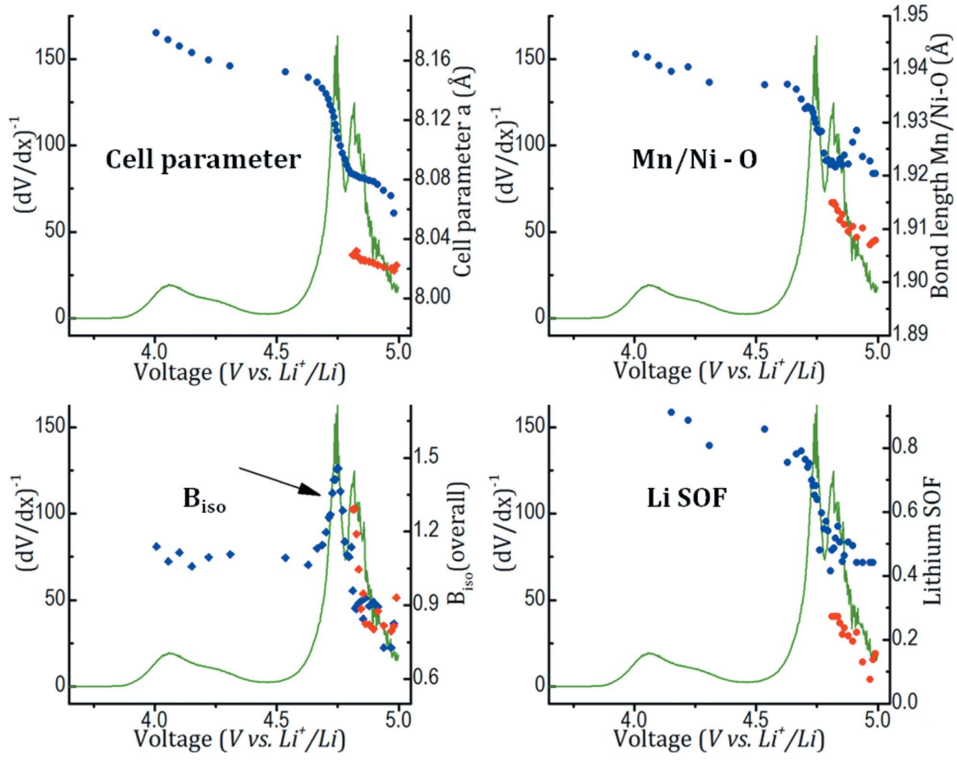


**Figure 6**
Structural parameters obtained from Rietveld refinements upon the charge of $LiNi_{0.4}Mn_{1.6}O_4$, plotted against voltage and matched with the inverse derivative $(dV/dx)^{-1}$ of the electrochemical curve.

For these reasons we performed a galvanostatic electrochemical cycle of a $LiMn_2O_4$//Li half-cell, while measuring synchrotron XRPD *operando*. We aimed at taking advantage of the great angular and intensity resolution available at the MSPD end station of the ALBA synchrotron facility (Barcelona; Fauth *et al.*, 2013). The battery was assembled using a custom *in situ* electrochemical cell developed in our groups for synchrotron *operando* studies (Leriche *et al.*, 2010). Galvanostatic cycling was performed at a C/6 rate in the extended voltage range between 3 and 4.8 V *versus* $Li^+$/Li, while measuring XRPD patterns every 5 min continuously. The results of this *operando* experiment are shown in Fig. 7. During charge one clearly notices an initial solid solution region, extending to $\sim Li_{0.6}Mn_2O_4$, followed by two topotactic biphasic reactions. This allowed us to isolate an intermediate cubic phase of cell parameter $a = 8.1529$ (1) Å (around $Li_{0.5}Mn_2O_4$) and a final one, known as λ-$MnO_2$, of cell parameter $a$ = 8.0363 (1) Å (shown in Fig. 8). Upon discharge the process is reversed, but not fully reversible. The lithiation, almost complete, could proceed to the composition $Li_{0.95}Mn_2O_4$ with $a$ = 8.2435 (1) Å, a value extremely close to the pristine one [$a$ = 8.2451 (1) Å]. However, importantly, the solid solution region is now found to be associated with the Li-poor phase λ-$MnO_2$ and not with the Li-rich one as was during charge (Fig. 7). Note that the asymmetric behaviour of $LiMn_2O_4$ has already been observed for example by Baehtz *et al.* (2005), but this is the first time it is detailed with high angular and time resolution.

Fig. 9 compares the Bragg peaks in the pristine state with their counterpart after one and two *in situ* cycles were carried out. The peaks' shape clearly evolves upon the first cycle, while almost no evolution is observed between the first and the second cycle: the shapes of diffracted peaks become

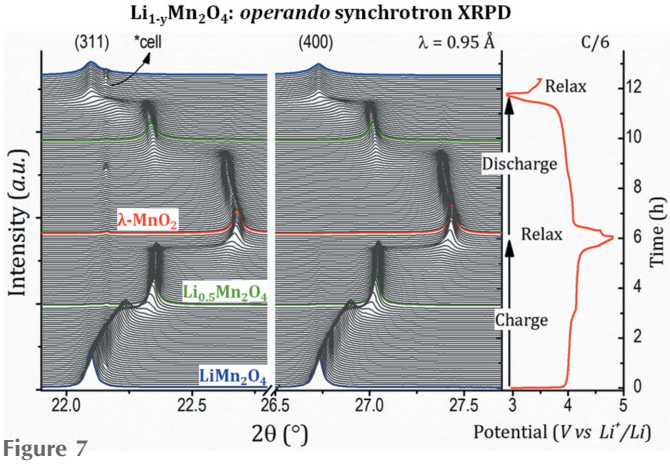


**Figure 7**
Evolution of (311) and (400) Bragg reflections of $LiMn_2O_4$ during a full electrochemical cycle of an $LiMn_2O_4$//Li half-cell, observed by *operando* synchrotron XRPD. Two topotactic biphasic reactions are present upon charge and discharge.

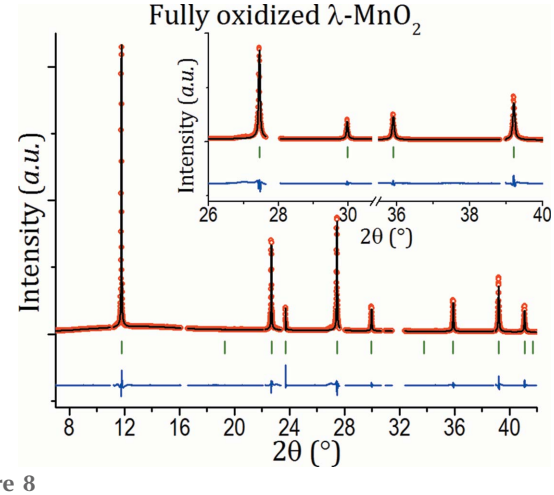


**Figure 8**
Rietveld refinements of *operando* synchrotron XRPD of the end-member λ-$MnO_2$ obtained after a full galvanostatic charge of the $LiMn_2O_4$//Li half-cell. Excluded regions account for reflections from the cell setup, metallic lithium, PTFE binder, beryllium windows and their protective aluminium layer.

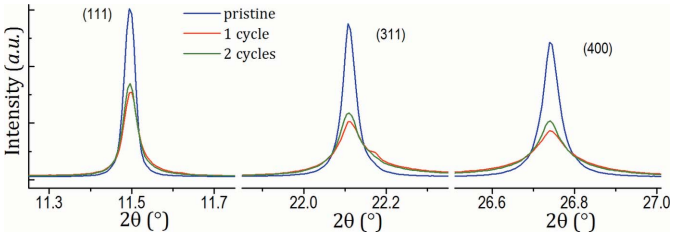


**Figure 9**
(111), (311) and (400) Bragg reflections of $LiMn_2O_4$ in the pristine state and after the first and second electrochemical cycle from *operando* synchrotron XRPD data.

significantly more Lorentzian and a careful observation of the diffraction scans reveals a continuous broadening, starting from the very first ones. Therefore, the phenomenon is not related to some reaction happening at high voltage, but it proceeds continuously throughout charge and discharge. The broadening we observe here, created during the first cycle, is not a simple increase in peak's FWHM, which is indeed rather constant. Instead, the peak shape function after the first electrochemical cycle tends towards a pure Lorentzian function. It is clearly shown in Fig. 9 by the occurrence of extended tails at the base of Bragg reflections and the effect is so significant that the observed peaks can no longer be modelled using a single mathematical function. They have to be described as so-called super-Lorentzian shaped, *i.e.* two Lorentzian peaks, one narrow and one very broad, centred at the same angular position (Young & Sakthivel, 1988). From the physical point of view this means that we postulate the presence of several 'phases', very close in composition (and cell parameters *etc.*) but with a bimodal distribution of coherent domain sizes. The two Lorentzian peaks will then give the two most representative domain sizes. A slight asymmetry in peak shapes is also observed in Fig. 9, indicating that this distribution of domains which is different in size might be related to under-lithiated regions of the electrode. This effect, which is secondary, could not be taken into account in addition to the super-Lorentzian shape due to limitations in the stability of the Rietveld refinement.

From a practical point of view, the 'two phases' we used in the Rietveld refinements only differ by their isotropic size parameter. One finds that in the pristine state there is essentially no broadening due to size effects (obtained particle size > 100 nm), while after one cycle the extremes of the domain size distribution are well identified: one is pristine-like (not broadened) and a second one, from the very broad peaks' tails, corresponds to an apparent domain size of 9.2 (1) nm. The 'two phases' appear to be in a ∼ 2:1 ratio and we can conclude that at the end of the first cycle about 66% of $LiMn_2O_4$ maintains the same crystallinity, while the other 34% has a significantly reduced coherent domain size, decreasing down to 9.2 (1) nm. If the same refinement is performed in the middle of the first cycle, *i.e.* at the end of charge, one similarly finds that the fraction with reduced domain size is already of 20%, for a domain size which is similar, *i.e.* 9.9 (1) nm. Whether this effect is due to the creation of several small domains within the particles or at the interfacial region is an issue that cannot be addressed by XRPD, but will be further investigated using TEM.

One matter that can instead be addressed by our *operando* XRPD experiment is the nature of the intermediate $Li_{0.5}Mn_2O_4$ phase. Two intense Bragg peaks are already shown in Fig. 7, but even more important clues about the existence of a new phase lie in the observation of weak reflections, as shown in Fig. 10. Several points deserve to be highlighted:

(i) The (111) diffracted peak is the most intense one for spinels, due to the high packing density of Mn cations in this family of planes. It shows the same behaviour already observed for (311) and (400) in Fig. 7, *i.e.* only partial reversibility.

(ii) The (220) reflection is interesting as it is strongly correlated in spinels with the scattering power of the atom in the tetrahedral site 8*a* (Barth & Posnjak, 1932). In this case this atom is lithium, meaning that the reflection is already very weak in the pristine state and that it

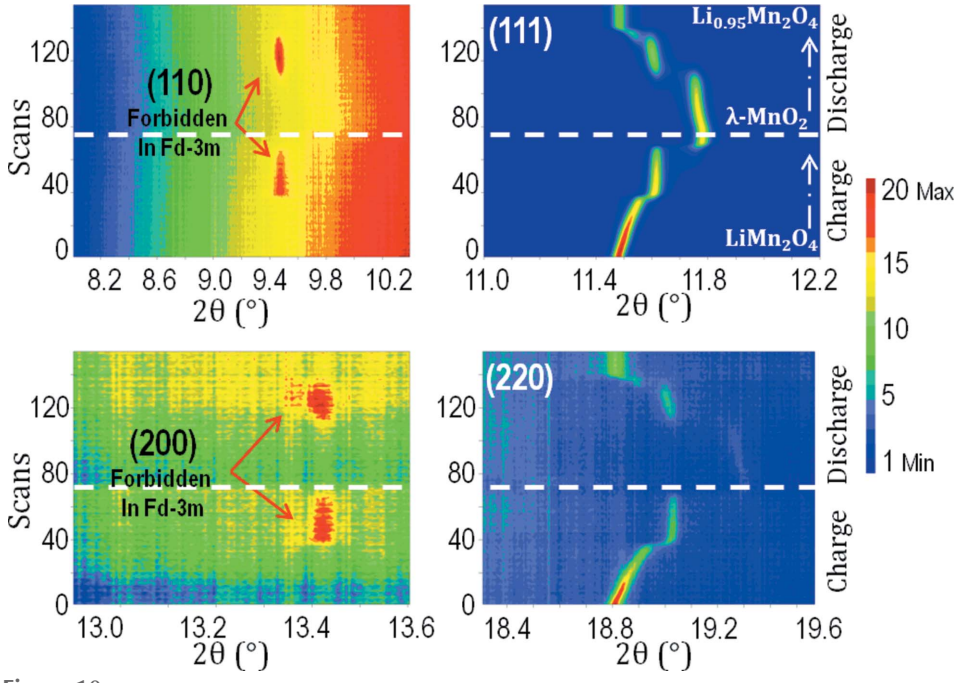


**Figure 10**
Contour plots of significant Bragg reflections observed upon electrochemical cycling of $LiMn_2O_4$ from *operando* synchrotron XRPD. On the right, the evolution of the most intense peak (111) is reported, together with the (220) one, both always present during the experiment [although (220) almost loses all its intensity in the delithiated phase]. On the left, (110) and (200) reflections are observed for the intermediate phase only, both during charge and discharge, implying a symmetry reduction.

**Table 1**
Structural parameters obtained from Rietveld refinement of $Li_{0.5}Mn_2O_4$.

(–) indicates that a value has not been refined in $P2_13$, but it was kept as refined in the $P4_332$ space group.

| | |
|---|---|
| $Li_{0.5}Mn_2O_4$ (*in situ*) | |
| Space group: $P2_13$; $Z = 8$ | |
| $a = b = c = 8.1529$ (1) Å | $R_{Bragg} = 0.0806$ |
| $V = 541.92$ (1) Å$^3$; $V/Z = 67.74$ (1) Å$^3$ | $R_{wp} = 0.189$ |
| Main $Li_{0.5}Mn_2O_4$ phase = 96 (1) wt%; | $\chi^2 = 60.2$ |
| Secondary $LiMn_2O_4$-like phase = 3.3 (2) wt% [$Fd\bar{3}m$, $a$ = 8.2390 (4) Å] | |

| | | Atomic positions | | | | |
|---|---|---|---|---|---|---|
| Atoms | Wyckoff positions | *x*/*a* | *y*/*b* | *z*/*c* | Occ. | $B_{iso}$ |
| Mn1 | 4*a* | 0.626 (7) | 0.626 (7) | 0.626 (7) | 1 | 2.6 (–) |
| Mn2 | 12*b* | 0.128 (6) | 0.380 (4) | −0.127 (4) | 1 | 2.6 (–) |
| O1 | 4*a* | 0.387 (21) | 0.387 (21) | 0.387 (21) | 1 | 2.3 (–) |
| O2 | 12*b* | 0.142 (25) | −0.135 (16) | 0.136 (19) | 1 | 2.3 (–) |
| O3 | 4*a* | 0.869 (18) | 0.869 (18) | 0.869 (18) | 1 | 2.3 (–) |
| O4 | 12*b* | 0.104 (19) | 0.119 (16) | 0.396 (17) | 1 | 2.3 (–) |
| Li1 | 4*a* | 0.011 (–) | 0.011 (–) | 0.011 (–) | 1 | 1.0 (–) |

totally loses its intensity while approaching the λ-$MnO_2$ phase, to partially regain it afterwards when lithium is reinserted in the site.

(iii) The most important observation here is the presence of two reflections, (110) and (200), as indexed in the $P4_332$ or $P2_13$ space groups (the choice of space groups is discussed later). They appear in the middle of charge and discharge, *i.e.* around composition $Li_{0.5}Mn_2O_4$. These reflections are forbidden in the $Fd\bar{3}m$ space group of the pristine spinel. They are observed here for the first time and they are extremely important because they hold the key to revealing and understanding the symmetry/ordering within $Li_{0.5}Mn_2O_4$.

The presence of the (110) reflection can be understood by using an analogy with another spinel-based material, $LiNi^{2+}_{0.5}Mn^{4+}_{1.5}O_4$. In this composition, a classical cation-disordered structure can turn into an ordered one where the $Ni^{2+}$:$Mn^{4+}$ (1:3) ratio leads to a reduction in space-group symmetry, from $Fd\bar{3}m$ to $P4_332$, hence allowing the presence of the (110) reflection (Kim *et al.*, 2004; Amdouni *et al.*, 2006; Wang *et al.*, 2011). It is interesting to notice that $Li_{0.5}Mn_2O_4$ can indeed be written as $Li_{0.5}Mn^{3+}_{0.5}Mn^{4+}_{1.5}O_4$, showing the same cation ratio (1:3) as in $LiNi_{0.5}Mn_{1.5}O_4$. We applied this space-group reduction of $LiNi_{0.5}Mn_{1.5}O_4$ (ICSD 70045; Gryffroy *et al.*, 1991) to $Li_{0.5}Mn_2O_4$. The results of the structural Rietveld refinements displayed in Fig. 11 show how the (110) reflection is nicely fitted, taking into account the space group $P4_332$, enlightening for the first time an ordering between $Mn^{3+}$ and $Mn^{4+}$ cations in $Li_{0.5}Mn^{3+}_{0.5}Mn^{4+}_{1.5}O_4$ during charge and discharge of $LiMn_2O_4$, whenever they reach a ratio of 1:3. While these refinements perfectly account for the existence of the (110) Bragg peak, they still maintain the (200) one as forbidden. We hence envisaged possible Li/vacancy ordering at the composition $Li_{0.5}Mn^{3+}_{0.5}Mn^{4+}_{1.5}O_4$ using a further space-group symmetry reduction. In fact, in $P4_332$ all lithium ions are placed in the same 8*a* site, which must therefore be only half occupied to respect the stoichiometry. Among the cubic subgroups of $P4_332$, $P2_13$ allows the 1:3 cations ratio to be maintained, while reducing the multiplicity of the tetrahedral lithium site to 4*a* in such a way that that newly defined lithium site is full, whereas that corresponding to the vacancies is obviously empty. In the $P2_13$ space group, systematic conditions for extinctions allow the presence of both the (110) and (200) reflections, as illustrated in Fig. 11.

Tables 1 and 2 gather and compare the structural information obtained for $Li_{0.5}Mn_2O_4$ in both the $P4_332$ and $P2_13$ space groups, while the arrangements of cations and lithium/vacancy ordered distributions in $Li_{0.5}Mn_2O_4$ are displayed in Fig. 12. As already well documented in the literature, the oxygen c.c.p.-based (cubic close packed) spinel structure can be described as a stacking of two types of cations layers, referred to as $[O_h]_3$ (Mn-rich, with 3 octahedral ($O_h$) sites occupied and 1 $O_h$ empty) and $[T_d]_2[O_h]$ [Li-rich, with 2 tetrahedral ($T_d$) sites occupied, 1 $O_h$ occupied and 3 $O_h$ vacant], perpendicular to the $[111]_{cubic}$ direction. Importantly, $Mn^{3+}$ and $Mn^{4+}$ are present in the two types of layers (in an ordered fashion respecting in both cases the 1:3 ratio) and are also ordered along the [111] direction. The red circles in Fig. 12 show how

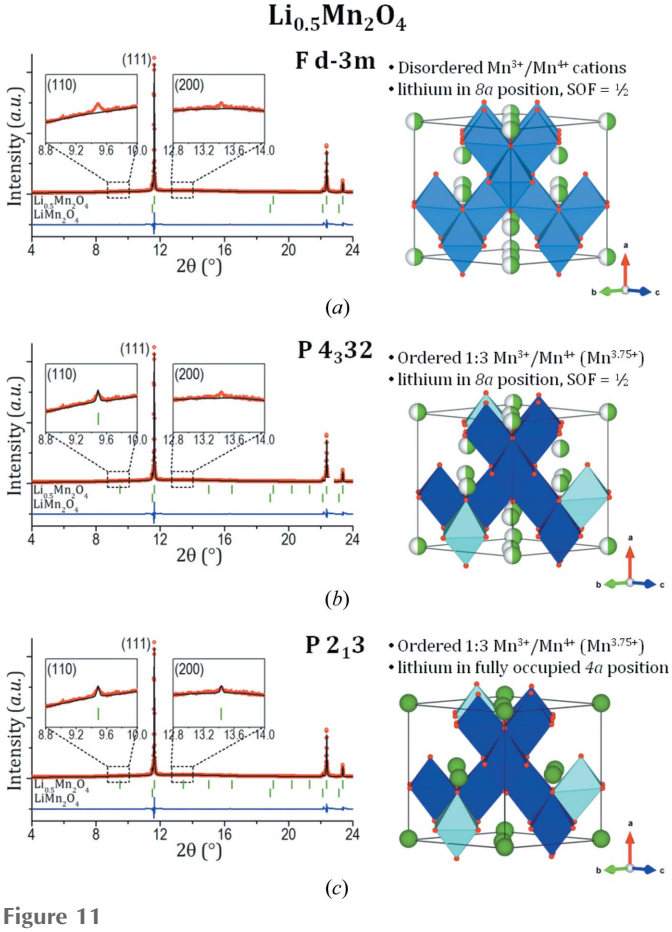


**Figure 11**
Rietveld refinements of *operando* synchrotron XRPD data for the phase $Li_{0.5}Mn_2O_4$ obtained during galvanostatic cycling of $LiMn_2O_4$. (*a*) Pristine-like space group $Fd\bar{3}m$. (*b*) Cation-ordered $P4_332$. (*c*) Cation- and lithium/vacancy-ordered $P2_13$. Respective crystal structures are displayed. Insets focus on 8.8–10.0° and 12.8–14.0° angular ranges. A secondary pristine $LiMn_2O_4$-like phase is added in the refinements (≃ 3 wt%) because of the dynamic *operando* conditions.

layers are stacked: a $Mn^{3+}$ cation in the Li-rich layer is always on top of 3 $Mn^{4+}$ cations in the Mn-rich layer. Even though the obtained values of Mn—O bond lengths gathered in Table 2 (for $P2_13$) show significant error bars, the environments around Mn2 ($Mn^{4+}$, with most Mn—O bonds in the range 1.90–1.94 Å) and Mn1 ($Mn^{3+}$, with longer Mn—O bonds in the range 1.94–2.01 Å) clearly enlighten the presence of two Mn environments, further supported by bond-valence sum calculations (Fig. 13). It is noteworthy that this bonds' distribution around Mn1 (3 + 3) is not compatible with a 'classical' Jahn–Teller distortion of the $Mn^{3+}$ cation (4 + 2) that one could expect. First-principles calculations (applied to $Li_2Mn_2O_4$; Van der Ven *et al.*, 2000) indicated that a compression of the $Mn^{3+}$—O bond can lead to a favourable low-spin configuration, where the $e_g$ electron is instead placed as the fourth electron in the $t_{2g}$ energy levels (crystal field energy lower than exchange energy). This could be the case here because of the constraints applied by the surrounding $Mn^{4+}$ cations on a central $Mn^{3+}$ one, possibly explaining the missing Jahn–Teller distortion. An analogous effect had been observed for $Ni^{3+}$ cations in $LiNi_{0.3}Co_{0.7}O_2$ (Mansour *et al.*, 2005).

As previously mentioned, the $P2_13$ space group is well suited to support lithium/vacancy ordering. Lithium is located in the 8*a* site in $Fd\bar{3}m$ and $P4_332$ space groups, while it is located in the 4*a* one in $P2_13$. This site, once filled, represents only half of those partially occupied within the previous space groups, and it satisfies the stoichiometry of $Li_{0.5}Mn_2O_4$. This ordering scheme is the same one that was predicted by Van der Ven *et al.* (2000) through computational methods, with lithium and vacancies alternated along the [110] direction (as can be seen at the bottom of Fig. 11). However, *a priori*, the distribution of lithium and vacancies could be reversed (translation by $\frac{3}{4}, \frac{1}{4}, \frac{3}{4}$) and we cannot determine yet any preference for one or the other lithium/vacancy ordering. Additional considerations regarding the possible minimization of electrostatic repulsions fail because for both lithium/vacancy distributions lithium ions have in their vicinity (0–3.5 Å) 12 manganese cations of which 3 $Mn^{3+}$ and 9 $Mn^{4+}$ have similar bond lengths. We left the Li position constant to the value reported in the literature for $LiNi_{0.5}Mn_{1.5}O_4$, knowing that $x = y = z = 0.011$ in $P4_332$ is very close to $x = y = z = 0$ in $Fd\bar{3}m$ of the classic spinel.

As a conclusive remark, we think it is possible that the $P2_13$ space group is the correct representation for the composition $Li_{0.5}Ni^{3+}_{0.5}Mn^{4+}_{1.5}O_4$. In fact, pristine $LiNi_{0.5}Mn_{1.5}O_4$ in the cation-ordered version already crystallizes in the $P4_332$ space group. As previously discussed (§3), upon $Li^+$ extraction it undergoes a biphasic topotactic reaction leading to the intermediate stable phase $Li_{0.5}Ni^{3+}_{0.5}Mn^{4+}_{1.5}O_4$. This composition

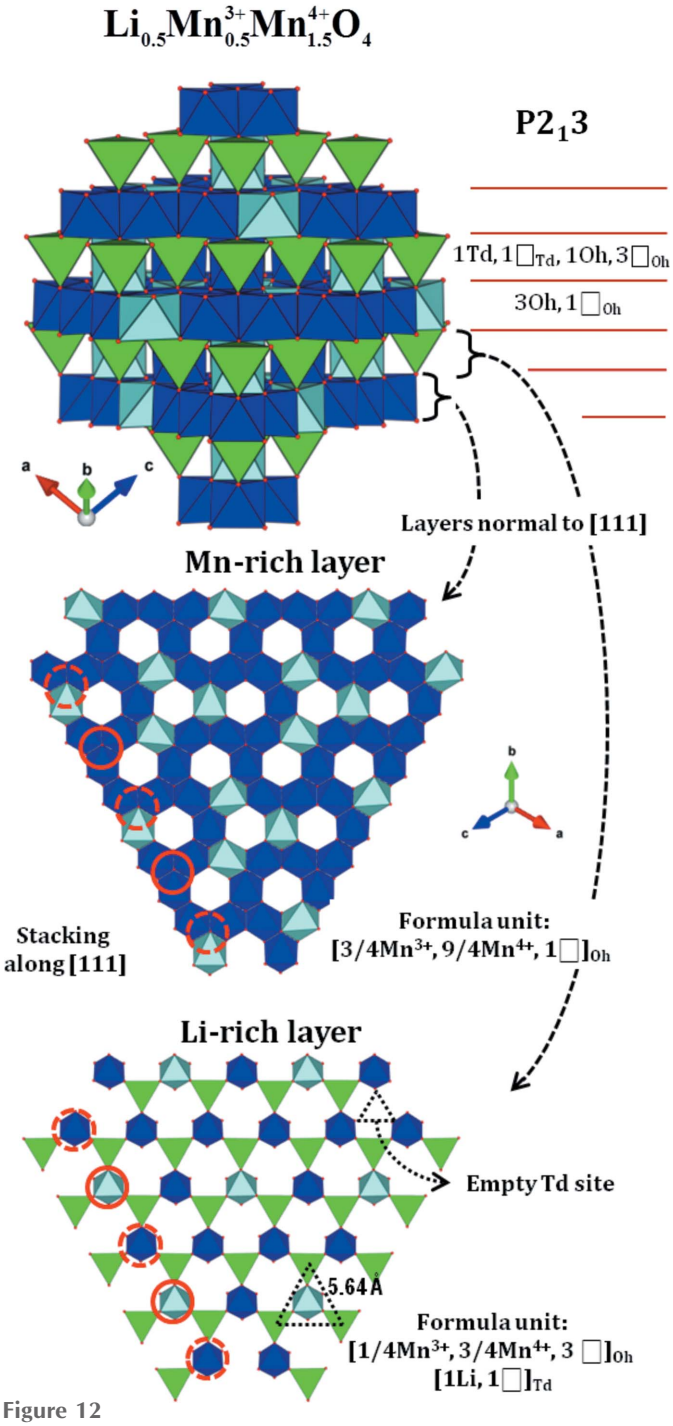


**Figure 12**
Representation of $Li_{0.5}Mn_2O_4$ along the [111] direction, showing oxygen layers and the alternating manganese-rich and lithium-rich layers. Dark blue octahedra represent $Mn^{4+}$, light blue ones $Mn^{3+}$ and green tetrahedra lithium. At the bottom, isolated Mn-rich and Li-rich layers, seen normal to [111]. The full/dashed red circles are a visual guide for the vertical stacking of layers, namely the Li-rich one can be shifted to the top until the circles coincide.

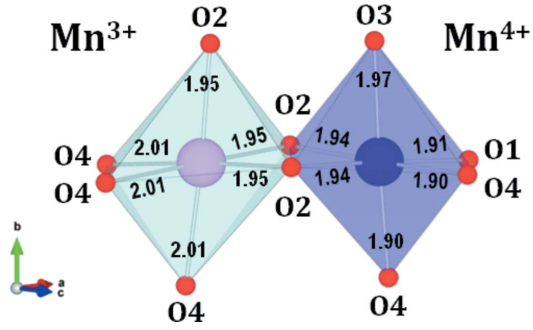


**Figure 13**
Bond lengths of $Mn^{3+}$—O and $Mn^{4+}$—O octahedra.

**Table 2**
Significant bond length distances (Å) obtained from Rietveld refinement of $Li_{0.5}Mn_2O_4$ in the $P2_13$ space group, compared with those obtained for the $P4_332$ one.

Error bars are reported as $3\sigma$. Polyhedral distortion is calculated as $\Delta = \frac{1}{N}\sum_{i=1}^{N}\left(\frac{d_i - \langle d\rangle}{\langle d\rangle}\right)^2$, bond valences as reported in Brown & Altermatt (1985).

| | | O1 | O2 | O3 | O4 | BVS | Distortion |
|---|---|---|---|---|---|---|---|
| $Li_{0.5}Mn_2O_4$ ($P2_13$ *versus* $P4_332$) | | | | | | | |
| Mn1 | $P2_13$ | – | 1.94 (15) ×3 | – | 2.01 (15) ×3 | 3.3 (6) | 2.9E-4 |
| | $P4_332$ | – | 1.99 (4) ×6 | – | – | 3.2 (2) | 0.001E-4 |
| Mn2 | $P2_13$ | 1.91 (18) | 1.94 (18) ×2 | 1.97 (15) | 1.90 (15) ×2 | 3.8 (6) | 2E-4 |
| | $P4_332$ | 1.92 (7) ×2 | 1.94 (5) ×2<br>1.90 (4) ×2 | – | – | 3.8 (2) | 0.839E-4 |
| Li | $P2_13$ | – | 1.90 (18) ×3 | 2.00 (18) | – | 1.2 (3) | 6E-4 |
| | $P4_332$ | 2.08 (7) | 1.92 (4) ×3 | – | – | 1.07 (7) | 11E-4 |

possesses the same 1:3 cation ratio and the same lithium/vacancy ratio of $Li_{0.5}Mn_2O_4$. It thus seems reasonable that it could show the same ordering and space group belonging.

## 6. Conclusion

In this work we have provided a glimpse of the different possibilities available nowadays for *operando* diffraction studies on Li-ion batteries, focusing mainly on the great prospects of neutrons and synchrotron radiation. The advantages and drawbacks of both probes are discussed, reviewing the development of custom electrochemical cells specifically designed for such studies. New data were shown to support the benefits of both techniques. On one side, spinel materials of compositions $Li_{1+x}Mn_{2-x}O_4$ ($0 \leq x \leq 0.10$) and $LiNi_{0.4}Mn_{1.6}O_4$ were thoroughly investigated by *operando* neutron powder diffraction, unveiling several subtle details about the physics of the $Li^+$ insertion and extraction processes. These features are revealed thanks to the ability to exploit Rietveld refinements quantitatively for data analysis, in a reproducible way even for critical parameters as site occupancy factors and Debye–Waller factors. On the other side, the high angular and intensity resolution available at synchrotron radiation beamlines allow studying relatively well known materials, as for example $LiMn_2O_4$, and obtaining new insights on their behaviour upon electrochemical cycling. Importantly, we have shown that the material undergoes irreversible transformations already during the first cycle, likely connected to its poor long-term cyclability. Moreover, we have finally determined the nature of the elusive composition $Li_{0.5}Mn_2O_4$, obtained reversibly in the middle of charge and discharge. This phase exhibits a double ordering scheme, including $Mn^{3+}$:$Mn^{4+}$ (1:3) cation ordering and lithium/vacancy ordering, leading to a symmetry reduction of the space group from $Fd\bar{3}m$ to $P2_13$.

## Acknowledgements

Jean-François Colin and Sébastien Patoux from CEA (Grenoble, France) are acknowledged for providing the high-voltage spinel sample $LiNi_{0.4}Mn_{1.6}O_4$, as well as Ludovic Gendrin and Jean-Luc Laborier from ILL (Grenoble, France) for their help in the development of the neutron-transparent electrochemical cell. The ALBA synchrotron and ILL are acknowledged for gaining access to high resolution and high flux diffractometers, Bio-Logic for providing the cycler on-site at ILL and at ALBA to perform *in situ* and *operando* experiments, Région Aquitaine for financial support, and ILL for the PhD thesis of MB.

## References

Amatucci, G. G., Pereira, N., Zheng, T. & Tarascon, J.-M. (2001). *J. Electrochem. Soc.* **148**, A171–A182.
Amdouni, N., Zaghib, K., Gendron, F., Mauger, A. & Julien, C. M. (2006). *Ionics*, **12**, 117–126.
Amine, K., Tukamoto, H., Yasuda, H. & Fujita, Y. (1996). *J. Electrochem. Soc.* **143**, 1607–1613.
Amine, K., Tukamoto, H., Yasuda, H. & Fujita, Y. (1997). *J. Power Sources*, **68**, 604–608.
Andersson, A. S., Kalska, B., Häggström, L. & Thomas, J. O. (2000). *Solid State Ionics*, **130**, 41–52.
Andre, D., Kim, S.-J., Lamp, P., Lux, S. F., Maglia, F., Paschos, O. & Stiaszny, B. (2015). *J. Mater. Chem. A*, **3**, 6709–6732.
Arai, H., Sato, K., Orikasa, Y., Murayama, H., Takahashi, I., Koyama, Y., Uchimoto, Y. & Ogumi, Z. (2013). *J. Mater. Chem. A*, **1**, 10442–10449.
Armand, M. & Tarascon, J. M. (2008). *Nature*, **451**, 652–657.
Bacon, G. E. (1975). *Neutron Diffraction*, 3rd ed. London: Clarendon Press.
Baehtz, C., Buhrmester, T., Bramnik, N. N., Nikolowski, K. & Ehrenberg, H. (2005). *Solid State Ionics*, **176**, 1647–1652.
Balasubramanian, M., Sun, X., Yang, X. Q. & McBreen, J. (2001). *J. Power Sources*, **92**, 1–8.
Barth, T. F. W. & Posnjak, E. (1932). *Z. Kristallogr.* **82**, 325–341.
Berg, H., Rundlöv, H. & Thomas, J. O. (2001). *Solid State Ionics*, **144**, 65–69.
Bergstöm, Ö., Andersson, A. M., Edström, K. & Gustafsson, T. (1998). *J. Appl. Cryst.* **31**, 823–825.
Bianchini, M., Leriche, J. B., Laborier, J.-L., Gendrin, L., Suard, E., Croguennec, L. & Masquelier, C. (2013). *J. Electrochem. Soc.* **160**, A2176–A2183.
Bianchini, M., Suard, E., Croguennec, L. & Masquelier, C. (2014). *J. Phys. Chem. C*, **118**, 25947–25955.
Borkiewicz, O. J., Shyam, B., Wiaderek, K. M., Kurtz, C., Chupas, P. J. & Chapman, K. W. (2012). *J. Appl. Cryst.* **45**, 1261–1269.
Bragg, W. H. (1915). *Nature*, **95**, 561.
Brown, I. D. & Altermatt, D. (1985). *Acta Cryst.* B**41**, 244–247.
Cai, L., An, K., Feng, Z., Liang, C. & Harris, S. J. (2013). *J. Power Sources*, **236**, 163–168.
Chabre, Y. (1993). *NATO ASI Series*, Vol. 305, *Chemical Physics of Intercalation II*, edited by P. Bernier, J. Fischer, S. Roth & S. Solin, pp. 181–192. New York: Springer.
Chen, Z., Lu, Z. & Dahn, J. R. (2002). *J. Electrochem. Soc.* **149**, A1604–A1609.
Cho, J. & Thackeray, M. M. (1999). *J. Electrochem. Soc.* **146**, 3577–3581.
Colin, J. F., Godbole, V. & Novák, P. (2010). *Electrochem. Commun.* **12**, 804–807.
Croguennec, L. & Palacin, M. R. (2015). *J. Am. Chem. Soc.* **137**, 3140–3156.
Cuisinier, M., Cabelguen, P.-E., Evers, S., He, G., Kolbeck, M., Garsuch, A., Bolin, T., Balasubramanian, M. & Nazar, L. F. (2013). *J. Phys. Chem. Lett.* **4**, 3227–3232.
Dahn, J. R. (1991). *Phys. Rev. B*, **44**, 9170–9177.

Dahn, J. R. & Haering, R. R. (1981). *Solid State Commun.* **40**, 245–248.

Dahn, J. R., Py, M. A. & Haering, R. R. (1982). *Can. J. Phys.* **60**, 307–313.

Du, G. D., Sharma, N., Peterson, V. K., Kimpton, J. A., Jia, D. Z. & Guo, Z. P. (2011). *Adv. Funct. Mater.* **21**, 3990–3997.

Duncan, H., Hai, B., Leskes, M., Grey, C. P. & Chen, G. (2014). *Chem. Mater.* **26**, 5374–5382.

Erickson, E. M., Ghanty, C. & Aurbach, D. (2014). *J. Phys. Chem. Lett.* **5**, 3313–3324.

Fauth, F., Peral, I., Popescu, C. & Knapp, M. (2013). *Powder Diffr.* **28**, S360–S370.

Gao, Y., Myrtle, K., Zhang, M., Reimers, J. N. & Dahn, J. R. (1996). *Phys. Rev. B*, **54**, 16670–16675.

Godbole, V. A., Hess, M., Villevieille, C., Kaiser, H., Colin, J. F. & Novák, P. (2013). *RSC Adv.* **3**, 757–763.

Goodenough, J. B. & Kim, Y. (2010). *Chem. Mater.* **22**, 587–603.

Goodenough, B. J., Thackeray, M. M., David, F. W. I. & Bruce, G. P. (1984). *Lithium Insertion/Extraction Reactions with Manganese Oxides.* Paris: Gauthier-Villars.

Gryffroy, D., Vandenberghe, R. & Legrand, E. (1991). *Mater. Sci. Forum*, **79–82**, 785–790.

Gummow, R. J., de Kock, A. & Thackeray, M. M. (1994). *Solid State Ionics*, **69**, 59–67.

Harks, P. P. R. M. L., Mulder, F. M. & Notten, P. H. L. (2015). *J. Power Sources*, **288**, 92–105.

Isnard, O. (2007). *C. R. Phys.* **8**, 789–805.

Jumas, J.-C., Sougrati, M., Perea, A., Aldon, L. & Olivier-Fourcade, J. (2013). *Hyperfine Interact.* **217**, 107–115.

Kanno, R., Kondo, A., Yonemura, M., Gover, R., Kawamoto, Y., Tabuchi, M., Kamiyama, T., Izumi, F., Masquelier, C. & Rousse, G. (1999). *J. Power Sources*, **81–82**, 542–546.

Kim, J. H., Myung, S. T., Yoon, C. S., Kang, S. G. & Sun, Y. K. (2004). *Chem. Mater.* **16**, 906–914.

Koga, H., Croguennec, L., Ménétrier, M., Mannessiez, P., Weill, F., Delmas, C. & Belin, S. (2014). *J. Phys. Chem. C*, **118**, 5700–5709.

Kunduraci, M. & Amatucci, G. G. (2006). *J. Electrochem. Soc.* **153**, A1345–A1352.

Kunduraci, M. & Amatucci, G. G. (2008). *Electrochim. Acta*, **53**, 4193–4199.

Lee, E. & Persson, K. A. (2012). *Energy Environ. Sci.* **5**, 6047–6051.

Leriche, J. B., Hamelet, S., Shu, J., Morcrette, M., Masquelier, C., Ouvrard, G., Zerrouki, M., Soudan, P., Belin, S., Elkaïm, E. & Baudelet, F. (2010). *J. Electrochem. Soc.* **157**, A606–A610.

Liu, W., Kowal, K. & Farrington, G. C. (1998). *J. Electrochem. Soc.* **145**, 459–465.

Mansour, A. N., Croguennec, L. & Delmas, C. (2005). *Electrochem. Solid-State Lett.* **8**, A544–A548.

Martinez, S., Sobrados, I., Tonti, D., Amarilla, J. M. & Sanz, J. (2014). *Phys. Chem. Chem. Phys.* **16**, 3282–3291.

Masquelier, C. & Croguennec, L. (2013). *Chem. Rev.* **113**, 6552–6591.

Masquelier, C., Tabuchi, M., Ado, K., Kanno, R., Kobayashi, Y., Maki, Y., Nakamura, O. & Goodenough, J. B. (1996). *J. Solid State Chem.* **123**, 255–266.

Morcrette, M., Chabre, Y., Vaughan, G., Amatucci, G., Leriche, J. B., Patoux, S., Masquelier, C. & Tarascon, J. M. (2002). *Electrochim. Acta*, **47**, 3137–3149.

Mukerjee, S., Thurston, T. R., Jisrawi, N. M., Yang, X. Q., McBreen, J., Daroux, M. L. & King, X. K. (1998). *J. Electrochem. Soc.* **145**, 466–472.

Nishikawa, S. (1915). *Proc. Tokyo Math. Phys. Soc.* **8**, 199–209.

Ohzuku, T., Kitagawa, M. & Hirai, T. (1990). *J. Electrochem. Soc.* **137**, 769–775.

Pang, W. K., Alam, M., Peterson, V. K. & Sharma, N. (2014). *J. Mater. Res.* pp. 1–8.

Pang, W. K., Kalluri, S., Peterson, V. K., Dou, S. X. & Guo, Z. (2014). *Phys. Chem. Chem. Phys.* **16**, 25377–25385.

Pang, W. K. & Peterson, V. K. (2015). *J. Appl. Cryst.* **48**, 280–290.

Pang, W. K., Peterson, V. K., Sharma, N., Shiu, J.-J. & Wu, S. (2014). *Chem. Mater.* **26**, 2318–2326.

Pang, W. K., Sharma, N., Peterson, V. K., Shiu, J.-J. & Wu, S. (2014). *J. Power Sources*, **246**, 464–472.

Patoux, S., Daniel, L., Bourbon, C., Lignier, H., Pagano, C., Le Cras, F., Jouanneau, S. & Martinet, S. (2009). *J. Power Sources*, **189**, 344–352.

Patoux, S., Sannier, L., Lignier, H., Reynier, Y., Bourbon, C., Jouanneau, S., Le Cras, F. & Martinet, S. (2008). *Electrochim. Acta*, **53**, 4137–4145.

Petibon, R., Li, J., Sharma, N., Pang, W. K., Peterson, V. K. & Dahn, J. R. (2015). *Electrochim. Acta*, **174**, 417–423.

Ravnsbaek, D. B., Xiang, K., Xing, W., Borkiewicz, O. J., Wiaderek, K. M., Gionet, P., Chapman, K. W., Chupas, P. J. & Chiang, Y. M. (2014). *Nano Lett.* **14**, 1484–1491.

Rietveld, H. M. (1969). *J. Appl. Cryst.* **2**, 65–71.

Roberts, M., Biendicho, J. J., Hull, S., Beran, P., Gustafsson, T., Svensson, G. & Edström, K. (2013). *J. Power Sources*, **226**, 249–255.

Rodriguez, M. A., Ingersoll, D., Vogel, S. C. & Williams, D. J. (2004). *Electrochem. Solid-State Lett.* **7**, A8–A10.

Rodríguez-Carvajal, J. (1993). *Physica B*, **192**, 55–69.

Rosciano, F., Holzapfel, M., Scheifele, W. & Novák, P. (2008). *J. Appl. Cryst.* **41**, 690–694.

Rossi Albertini, V., Perfetti, P., Ronci, F., Reale, P. & Scrosati, B. (2001). *Appl. Phys. Lett.* **79**, 27–29.

Rossouw, M. H., de Kock, A., de Picciotto, L. A., Thackeray, M. M., David, W. I. F. & Ibberson, R. M. (1990). *Mater. Res. Bull.* **25**, 173–182.

Rougier, A., Delmas, C. & Chadwick, A. V. (1995). *Solid State Commun.* **94**, 123–127.

Rousse, G., Masquelier, C., Rodríguez-Carvajal, J., Elkaim, E., Lauriat, J. P. & Martínez, J. L. (1999). *Chem. Mater.* **11**, 3629–3635.

Saravanan, K., Jarry, A., Kostecki, R. & Chen, G. (2015). *Sci. Rep.* **5**, 8027.

Schober, H. (2014). *J. Neutron Res.* p. 17.

Sharma, N., Du, G. D., Studer, A. J., Guo, Z. P. & Peterson, V. K. (2011). *Solid State Ionics*, **199–200**, 37–43.

Sharma, N., Guo, X. W., Du, G. D., Guo, Z. P., Wang, J. Z., Wang, Z. X. & Peterson, V. K. (2012). *J. Am. Chem. Soc.* **134**, 7867–7873.

Sharma, N. & Peterson, V. K. (2012). *J. Solid State Electrochem.* **16**, 1849–1856.

Sharma, N. & Peterson, V. K. (2013). *J. Power Sources*, **244**, 695–701.

Sharma, N., Peterson, V. K., Elcombe, M. M., Avdeev, M., Studer, A. J., Blagojevic, N., Yusoff, R. & Kamarulzaman, N. (2010). *J. Power Sources*, **195**, 8258–8266.

Sharma, N., Yu, D. H., Zhu, Y. S., Wu, Y. P. & Peterson, V. K. (2013). *Chem. Mater.* **25**, 754–760.

Tarascon, J. M., Coowar, F., Amatuci, G., Shokoohi, F. K. & Guyomard, D. G. (1995). *J. Power Sources*, **54**, 103–108.

Tarascon, J. M. & Guyomard, D. (1993). *Electrochim. Acta*, **38**, 1221–1231.

Tarascon, J. M., McKinnon, W. R., Coowar, F., Bowmer, T. N., Amatucci, G. & Guyomard, D. (1994). *J. Electrochem. Soc.* **141**, 1421–1431.

Tarascon, J. M., Wang, E., Shokoohi, F. K., McKinnon, W. R. & Colson, S. (1991). *J. Electrochem. Soc.* **138**, 2859–2864.

Thackeray, M. M. (1997). *Prog. Solid State Chem.* **25**, 1–71.

Thackeray, M. M., David, W. I. F., Bruce, P. G. & Goodenough, J. B. (1983). *Mater. Res. Bull.* **18**, 461–472.

Thackeray, M. M., de Kock, A., Rossouw, M. H., Liles, D., Bittihn, R. & Hoge, D. (1992). *J. Electrochem. Soc.* **139**, 363–366.

Thackeray, M. M., Johnson, P. J., de Picciotto, L. A., Bruce, P. G. & Goodenough, J. B. (1984). *Mater. Res. Bull.* **19**, 179–187.

Thurston, T. R., Jisrawi, N. M., Mukerjee, S., Yang, X. Q., McBreen, J., Daroux, M. L. & Xing, X. K. (1996). *Appl. Phys. Lett.* **69**, 194–196.

Vadlamani, B., An, K., Jagannathan, M. & Chandran, K. S. R. (2014). *J. Electrochem. Soc.* **161**, A1731–A1741.

Van der Ven, A., Marianetti, C., Morgan, D. & Ceder, G. (2000). *Solid State Ionics*, **135**, 21–32.
Van Noorden, R. (2014). *Nature*, **507**, 26–28.
Villevieille, C., Sasaki, T. & Novák, P. (2014). *RSC Adv.* **4**, 6782–6789.
Wang, X. L., An, K., Cai, L., Feng, Z. L., Nagler, S. E., Daniel, C., Rhodes, K. J., Stoica, A. D., Skorpenske, H. D., Liang, C. D., Zhang, W., Kim, J., Qi, Y. & Harris, S. J. (2012). *Sci. Rep.* **2**, 747.
Wang, L. P., Li, H., Huang, X. J. & Baudrin, E. (2011). *Solid State Ionics*, **193**, 32–38.
Yang, Z., Zhang, J., Kintner-Meyer, M. C. W., Lu, X., Choi, D., Lemmon, J. P. & Liu, J. (2011). *Chem. Rev.* **111**, 3577–3613.
Yoon, W.-S., Grey, C. P., Balasubramanian, M., Yang, X.-Q. & McBreen, J. (2003). *Chem. Mater.* **15**, 3161–3169.
Young, R. A. & Sakthivel, A. (1988). *J. Appl. Cryst.* **21**, 416–425.
Zhong, Q. M., Bonakdarpour, A., Zhang, M., Gao, Y. & Dahn, J. R. (1997). *J. Electrochem. Soc.* **144**, 205–213.